Photoelectron Imaging Study of the Effect of Monohydration on O_2^- Photodetachment

F. Ahu Akin, Laura K. Schirra,† and Andrei Sanov*

Department of Chemistry, University of Arizona, Tucson, Arizona 85721-0041

Received: April 5, 2006; In Final Form: May 11, 2006

The photodetachment of the $O_2^-\cdot H_2O$ cluster anion at 780 and 390 nm is investigated in comparison with O_2^- using photoelectron imaging spectroscopy. Despite the pronounced shift in the photoelectron spectra, the monohydration has little effect on the photoelectron angular distributions: for a given wavelength and electron kinetic energy (eKE) range, the $O_2^-\cdot H_2O$ angular distributions are quantitatively similar to those for bare O_2^-. This observation confirms that the excess electron in $O_2^-\cdot H_2O$ retains the overall character of the $2p\pi_g^*$ HOMO of O_2^-. The presence of H_2O does not affect significantly the partial wave composition of the photodetached electrons at a given eKE. An exception is observed for slow electrons, where $O_2^-\cdot H_2O$ exhibits a faster rise in the photodetachment signal with increasing eKE, as compared to O_2^-. The possible causes of this anomaly are (i) the long-range charge−dipole interaction between the departing electron and the neutral $O_2\cdot H_2O$ skeleton affecting the slow-electron dynamics; and (ii) the s wave contributions to the photodetachment, which are dipole-forbidden for π_g^{-1} transitions in O_2^-, but formally allowed in $O_2^-\cdot H_2O$ due to lower symmetry of the cluster anion and the corresponding HOMO.

1. Introduction

Superoxide hydration has been the subject of many experimental and theoretical studies due to its fundamental importance as well as the role in biological[1,2] and atmospheric[3,4] processes. Much of the spectroscopic effort has focused on characterization of the structural and electronic properties of the $O_2^-(H_2O)_n$ cluster anions, aiming to understand: (i) the superoxide reactivity toward[5−9] and within[10−12] biologically relevant solvents; (ii) the interactions governing the water networks in clusters with an anionic core;[13,14] and (iii) the effect of solvation on photodynamics of superoxide.[15−19]

The object of this work, the superoxide monohydrate $O_2^-\cdot H_2O$, has been studied by photoelectron and photofragmentation spectroscopy and argon nanomatrix isolation methods. Johnson and co-workers reported the 355 nm (3.49 eV) photoelectron spectrum of $O_2^-\cdot H_2O$ containing two broad congested bands.[16] The polarization dependence of these bands is similar to that of the transitions accessing the $X\ ^3\Sigma_g^-$ and $a\ ^1\Delta_g$ neutral states in the photodetachment of bare superoxide.[16,20−23] The congestion of the $O_2^-\cdot H_2O$ spectrum is mainly due to the intermolecular degrees of freedom of the hydrated cluster and the dissociative nature of the electron detachment process, similar to other cases of cluster-anion photodetachment.[24−29]

Continetti and co-workers observed that the translational energy release to O_2 and H_2O neutral products in the dissociative photodetachment of $O_2^-\cdot H_2O$ were independent of the photon energy in the 2.37−4.74 eV range.[18] This result suggests that the electron detachment and cluster dissociation are uncoupled events. A later study by the same group also revealed that the Franck−Condon transition in $O_2^-\cdot H_2O$ photodetachment occurs to a weakly repulsive part of the intermolecular $O_2\cdot H_2O$ potential.[19]

The bonding motifs in the $O_2^-(H_2O)_n$ clusters were further investigated using argon nanomatrix isolation spectroscopy.[13,14] The hydration shell comprised of four water molecules around superoxide was characterized by probing the OH stretch region of the IR spectrum.[13] The presence of a free O−H stretch signature in the spectrum indicated that the $O_2^-\cdot H_2O$ cluster has C_s geometry, in which one of the hydrogens forms an ionic hydrogen bond with one of the O atoms in O_2^-, while the other maintains a cis configuration in the molecular plane.[14]

The $O_2^-\cdot H_2O$ anion has also been the subject of theoretical studies spanning over two decades, as part of an effort to explore the potential energy surface of the $O_2^-(H_2O)_n$ clusters.[30−43] The monohydrated cluster anion is predicted to have two low-lying structural isomers: the cis C_s isomer mentioned above and a C_{2v} symmetry structure in which the water molecule complexes with superoxide with both hydrogen atoms. The energetic ordering of these isomers has been a challenge to the available computational methods, mainly for the following reasons: (i) the electron correlation in the core O_2^- moiety requires a multireference wave function to be described properly; and (ii) the H-bonding interaction of O_2^- with water had to be treated at the same time. The consensus today is that with the inclusion of the zero-point energy the $O_2^-\cdot H_2O$ potential energy surface is rather flat and at room temperature the cluster has enough internal energy to convert from one isomeric form to the other.

In the planar $O_2^-\cdot H_2O$ complex, the degeneracy of the in and out-of-plane π^* orbitals of O_2^- is lifted. For the C_s isomer, this results in $^2A'$ and $^2A''$ electronic states, respectively. In their early work, Curtiss et al. determined that the $^2A''$ state is the ground state of $O_2^-\cdot H_2O$.[30] Using the QCISD(T) method, Buntine et al. calculated the $O_2^-\cdot H_2O$ ground and excited-state potential energy surfaces along the superoxide O−O stretch coordinate.[33] From the similarity of these surfaces to the corresponding O_2^- potentials, it was concluded that the excess electron resides in the frontier orbitals of O_2^-. Bell and Wright investigated the neutral $O_2\cdot H_2O$ geometry and energetics, in

* Corresponding author. E-mail: sanov@u.arizona.edu.

† National Science Foundation Research Experience for Undergraduates student, visiting from the Edinboro University of Pennsylvania, Edinboro, PA 16444 (Summer 2005).

10.1021/jp062135i CCC: $33.50
Published on Web 06/14/2006

addition to those of $O_2^-\cdot H_2O$, and found the neutral complex to be weakly bound and floppy.[35]

In this work, we report the results of a comparative study of $O_2^-\cdot H_2O$ and O_2^- photodetachment at 780 nm and in the vicinity of 390 nm using photoelectron imaging spectroscopy. In addition to photoelectron spectra, imaging provides photoelectron angular distributions (PADs) for all available electron kinetic energies (eKE) in a given experiment. The PADs are sensitive to the anion electronic structure and electron−neutral interactions governing the photodetachment process. In the following sections, we present the photoelectron spectra and eKE-dependent PADs for $O_2^-\cdot H_2O$ and O_2^- and interpret the results in the light of previous experimental and theoretical findings.

2. Experimental Section

The experiments were carried out using a negative ion photoelectron imaging spectrometer consisting of an ion source, a time-of-flight mass spectrometer, and a velocity-map photoelectron imaging[44] assembly, described in detail elsewhere.[45]

The $O_2^-\cdot H_2O$ clusters are generated by passing a 1:4 mixture of O_2 and argon over water at room temperature. The mixture is introduced into the source chamber through a pulsed nozzle (General Valve Series 9) operated at 70 Hz. The ions are synthesized by crossing the gas expansion 1−2 mm downstream with 1 keV electrons from an electron gun. Negative ions are extracted into the time-of-flight (TOF) region 15 cm downstream from the nozzle by the action of a repeller plate pulsed from 0 to −900 V. The ions pass through a 4 mm diameter aperture into the acceleration stack, where they are accelerated by additional +1950 V. After separating by mass in the 1.7 m long Wiley−McLaren[46] TOF region, ion mass spectra are recorded using a Chevron type 25 mm diameter dual microchannel plate (MCP) detector.

The ion packet of interest is intercepted by the photodetachment laser, and the resultant photoelectrons are detected using the velocity-map imaging technique.[44] The imaging assembly consists of a three-electrode lens and a μ-metal shielded electron flight tube (∼15 cm in length) mounted perpendicular to the ion and laser beams. The imaging detector consists of two 40 mm diameter microchannel plates and a phosphor screen (Burle, Inc.) monitored by a CCD camera (Roper Scientific, Inc.). The potential difference across the two microchannel plates, normally maintained at 1.0−1.2 kV, is pulsed to 1.8 kV for a 200 ns window, coinciding the electron arrival time to discriminate against background. For each image, background scans are acquired with the laser pulse timed to arrive 1 μs before the corresponding ion packet. The raw images are sent to the computer after being averaged for ∼20 000 experimental cycles.

In this work, the fundamental (1 mJ/pulse) or frequency doubled (160 μJ/pulse) output of an amplified Ti:Sapphire femtosecond laser system (Spectra Physics, Inc.) was used for photodetachment. The linearly polarized 780 or 390/396 nm laser beam was mildly focused using a 2 m focal length lens positioned ∼1.3 m before the laser beam crosses the ion beam. The average widths of the spectral and time envelopes of the laser pulses were 5.5 nm and 90 fs, respectively.

After the background subtraction, the photoelectron images were centered and averaged over several experimental runs. From the images, the original three-dimensional photoelectron distributions were reconstructed via the inverse Abel transform[47] using the BASEX protocol of Reisler and co-workers.[48] Integration of the signal intensity over a specific radial range yields the PADs, $I(\theta)$, which are described by the anisotropy parameter, β(eKE), according to the standard expression: $I(\theta) \propto 1 + \beta\cdot P_2(\cos\theta)$. The photoelectron spectra were obtained from the velocity distributions; the photodetachment transitions in O_2^- were used for the energy calibration. At each wavelength, the analysis has been performed on data sets from several different days.

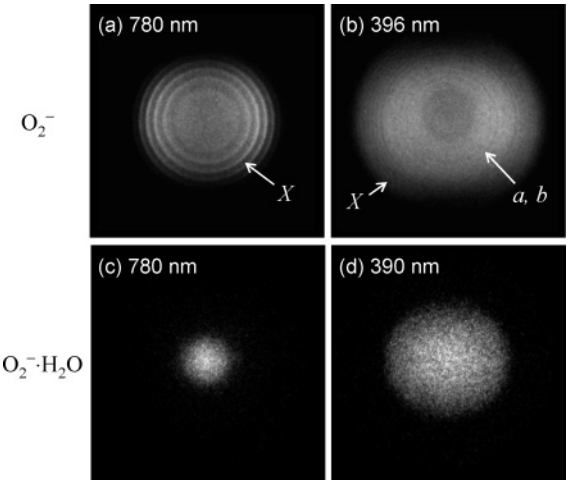

Figure 1. (a) Photoelectron image of O_2^- obtained at 780 nm (1.59 eV). The rings in the image correspond to the vibrationally resolved $X\ ^3\Sigma_g^- \leftarrow O_2^-\ X\ ^2\Pi_g$ transitions. (b) O_2^- image at 396 nm (3.13 eV), showing overlapping transitions to the $X\ ^3\Sigma_g^-$, $a\ ^1\Delta_g$, and $b\ ^1\Sigma_g^+$ electronic states of the neutral. (c) $O_2^-\cdot H_2O$ image at 780 nm (1.59 eV). (d) $O_2^-\cdot H_2O$ image at 390 nm (3.18 eV). All images are shown on arbitrary intensity and velocity scales (see Figures 2 and 3 for quantitative information). The laser polarization direction is vertical in the plane of all images shown.

3. Results and Modeling

The ground $X\ ^2\Pi_g$ state of O_2^- arises from the following electron configuration: $...(2s\sigma_g)^2(2s\sigma_u^*)^2(2p\sigma_g)^2(2p\pi_u)^4(2p\pi_g^*)^3$. Removal of an electron from the $2p\pi_g^*$ highest occupied molecular orbital (HOMO) yields the $X\ ^3\Sigma_g^-$, $a\ ^1\Delta_g$, and $b\ ^1\Sigma_g^+$ electronic states of O_2, with the $0 \leftarrow 0$ transitions corresponding to electron binding energies (eBE) of 0.448 ± 0.006,[21] 1.4262,[49−51] and 2.072 eV,[49,52,53] respectively.

Figure 1a and b shows the photoelectron images recorded in the photodetachment of O_2^- at 780 nm (1.59 eV) and 396 nm (3.13 eV), respectively. The results for $O_2^-\cdot H_2O$ at 780 and 390 nm are displayed in Figure 1c and d, respectively. At 780 nm, mainly the $X\ ^3\Sigma_g^-$ neutral state is accessed in the photodetachment of O_2^-, with the contribution from the $a\ ^1\Delta_g$ state origin in the small-eKE part of the spectrum. The image in Figure 1a exhibits six easily identifiable rings, corresponding to transitions to the $X\ ^3\Sigma_g^-$ ($v' = 0-5$) state of O_2 from the ground electronic and vibrational state of the anion, $X\ ^2\Pi_g$ ($v'' = 0$). The outermost (i.e., highest-eKE) ring in Figure 1a is assigned to the $0 \leftarrow 0$ transition.

The photoelectron spectrum obtained from the 780 nm O_2^- photoelectron image is shown in Figure 2a by a bold line. As compared to the past photoelectron spectroscopy experiments on O_2^-, such as, for example, the extensive study by Ervin and co-workers,[21] the spectrum in Figure 2a is characterized by much lower resolution. On the other hand, the imaging approach affords an important advantage of detecting the electrons all the way down to eKE = 0 with equal sensitivity. This capability is instrumental in examining the signal scaling in the low-eKE range.

The spectrum in Figure 2a includes contributions from the following vibronic transitions that are energetically allowed in

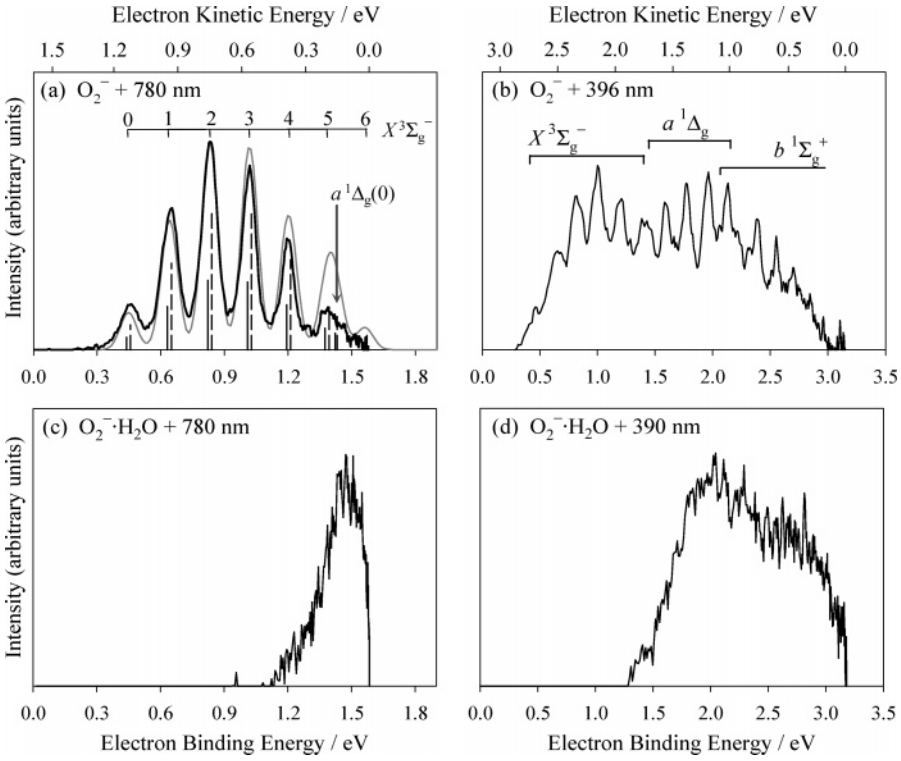

Figure 2. Photoelectron spectra of O_2^- and $O_2^-\cdot H_2O$, as indicated, obtained from the photoelectron images shown in Figure 1. In (a), the experimental O_2^- + 780 nm spectrum (bold line) is compared to a Franck−Condon simulation (thin line). The $J = {}^1/_2$ and ${}^3/_2$ spin−orbit components of the $X\,^3\Sigma_g^-$ ($v' = 0-6$) ← $X\,^2\Pi_{g,J}$ ($v'' = 0$) and $a\,^1\Delta_g$ ($v' = 0$) ← $X\,^2\Pi_{g,J}$ ($v'' = 0$) transitions are indicated by the simulated stick spectrum, weighted according to the corresponding Franck−Condon factors and $(2J + 1)$ degeneracy. The simulated spectrum is obtained by the convolution of the stick spectrum with a 39 meV wide Gaussian broadening function, as described in the text.

TABLE 1: Spectroscopic Constants of O_2

	$O_2^-(X\,^2\Pi_g)$	$O_2(X\,^3\Sigma_g^-)$	$O_2(a\,^1\Delta_g)$
r_e (Å)	1.348 ± 0.008	1.2075	1.2155
ω_e (cm^{-1})	1108 ± 20	1580.1	1509.8
$\omega_e\chi_e$ (cm^{-1})	9	11.9	13.1
spin−orbit constant, A (cm^{-1})	−153 ± 11		
EA_0 (eV)		0.448 ± 0.006	
T_0 (eV)	0	0	0.9773
references	21	49,80	49−51

780 nm (1.59 eV) photodetachment of O_2^-: $X\,^3\Sigma_g^-$ ($v' = 0-6$) ← $X\,^2\Pi_g$ ($v'' = 0$) and $a\,^1\Delta_g$ ($v' = 0$) ← $X\,^2\Pi_g$ ($v'' = 0$). Each of these transitions includes unresolved contributions from the $J = {}^1/_2$ and ${}^3/_2$ spin−orbit components of the $X\,^2\Pi_{g,J}$ state of the anion.

The experimental spectrum is compared to a Franck−Condon (FC) simulation indicated by a thin line in Figure 2a. The simulation takes into account the FC factors scaled by the $(2J + 1)$ degeneracies of the separate $J = {}^1/_2$, ${}^3/_2$ components of the $X\,^2\Pi_{g,J}$ ($v'' = 0$) anion state, while assuming equal electronic transition matrix elements for all observed lines. The line positions represented by the stick spectrum in Figure 2a are determined from the known spectroscopic constants of O_2 and O_2^-, while the FC factors are calculated using the vibrational wave functions corresponding to approximate Morse potentials for O_2^- and O_2. The spectroscopic constants and Morse potential parameters used in the simulation are summarized in Table 1. To account for the experimental resolution, the stick spectrum is convoluted with a Gaussian function, for which the optimal width (defined at half-maximum) is determined to be 39 meV.

While the experimental line positions are in agreement with the known spectroscopic properties of O_2^- and O_2,[21] in Figure 2a there is a mismatch between the observed and predicted line intensities. The relative scaling of the experimental and simulated spectra shown in the figure is arbitrarily adjusted to match the heights for the most intense peak, corresponding to the $X(2)$ ← $X(0)$ transition. Comparing the spectra, it appears that the FC simulation overestimates the intensity of the low-eKE peaks. We attribute this discrepancy to the electronic effects not accounted for in the FC model, the effect of the centrifugal barrier on the effective potential describing the interaction of the detached electron with the remaining neutral molecule. The barrier manifests in the Wigner-type[54] threshold behavior of the negative-ion photodetachment cross-sections[55−57] and has the effect of suppressing the detachment signal in the low-eKE regime. For example, as a result of the centrifugal suppression, the observed intensity of the combined $X(5)$ ← $X(0)$ and $a(0)$ ← $X(0)$ transitions is less than one-half of the FC prediction, while the $X(6)$ ← $X(0)$ line, expected at eBE = 1.56 eV (eKE = 0.03 eV),[21] is essentially not seen at all. As expected, the discrepancy between the experimental spectrum and the FC simulations gradually diminishes with increasing eKE.

The photodetachment of O_2^- at 396 nm accesses the $X\,^3\Sigma_g^-$, $a\,^1\Delta_g$, and $b\,^1\Sigma_g^+$ states of the neutral. The corresponding bands are indicated with arrows *X*, *a*, and *b* in Figure 1b. The photoelectron spectrum extracted from the 396 nm image and shown in Figure 2b contains partially overlapping contributions of the above electronic states.

As evident from Figure 1a,b, the O_2^- photoelectron angular distributions tend to peak in the direction perpendicular to the laser polarization axis at high electron kinetic energies, becoming more isotropic with decreasing eKE. The corresponding values of the anisotropy parameter β are summarized in Figure 3. In Figure 3a, the β values for O_2^- obtained at 780 nm are compared to the predictions of the Cooper−Zare central-potential model.[58,59] In the one-electron approximation, the

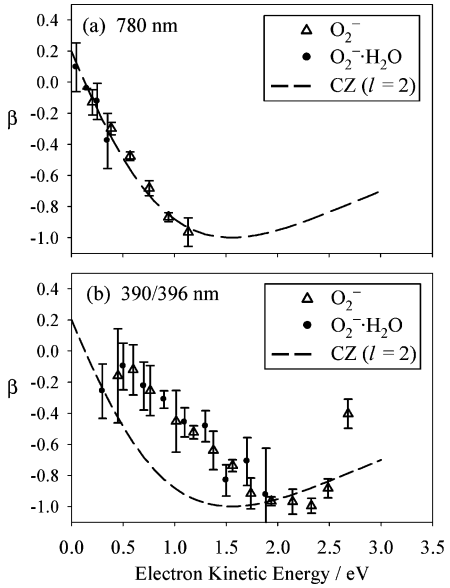

Figure 3. The eKE-dependent values of anisotropy parameter β obtained from the following photoelectron images: (a) O_2^- and O_2^-·H_2O at 780 nm; (b) O_2^- at 396 nm and O_2^-·H_2O at 390 nm. The error bars correspond to the 2σ uncertainty determined from analysis of multiple data sets obtained on different days. In (a), the dashed line represents the least-squares fit to the experimental data for O_2^- using the Cooper−Zare central-potential model for detachment from a d-like ($l = 2$) parent orbital, as described by eq 1. The same curve is reproduced unchanged in (b), for comparison with 396 nm data.

observed photodetachment transitions originate from the $2p\pi_g^*$ HOMO of O_2^-, which can be described as a d-like orbital with an effective angular momentum quantum number $l = 2$.[22] Within the Cooper−Zare model, the β(eKE) dependence for photoelectrons originating from this orbital is given by:[58−60]

$$\beta(\epsilon) = 2(1 + 6A_3^2\epsilon^2 - 18A_3\epsilon\cos(\delta_3 - \delta_1))/(10 + 15A_3^2\epsilon^2) \quad (1)$$

where $\epsilon \equiv$ eKE, while $A_3\epsilon = R_3/R_1$ is the ratio of the dipole radial matrix elements for the $l = 3$ and 1 partial waves, with $\delta_3 - \delta_1$ being the corresponding phase difference.[60] The phase difference determines the depth of the β(eKE) minimum. Because the experimental β values approach −1.0 at eKE = 1.1 eV, we set the phase shift between the outgoing p and f waves to zero: $\delta_3 - \delta_1 = 0$. The remaining model parameter, A_3, is used to fit eq 1 to 780 nm data. The least-squares fit corresponding to $A_3 = 0.42 \pm 0.02$ eV^{-1} is shown in Figure 3a by a dashed curve.

In the Cooper−Zare model, A_3 is a measure of the anion size.[60] Therefore, one might expect it to be independent of photon energy. If this were the case, the photodetachment anisotropy data should follow the same common β(eKE) trend, independent of the wavelength used. This argument works fairly well in some cases, such as, for example, bare and solvated I^- photodetachment.[28,61] To test the applicability of this hypothesis to superoxide, in Figure 3b we compare the β values for O_2^- obtained at 396 nm to the 780 nm Cooper−Zare fit curve reproduced from Figure 3a. Clearly, the 396 nm data do not follow the curve obtained by fitting eq 1 to the 780 nm data. This behavior, observed in O_2^- photodetachment at different wavelengths, will be discussed in a separate publication.

The 780 nm photoelectron image of O_2^-·H_2O, shown in Figure 1c, is different from that of O_2^- in Figure 1a in that it spans a much narrower eKE range and exhibits no discernible vibrational structure. The vibrational structure is also lacking

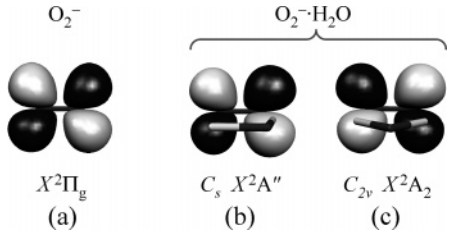

Figure 4. Amplitude plots of the highest occupied molecular orbitals of O_2^- and two isomeric forms of the O_2^-·H_2O cluster anion, corresponding to C_s and C_{2v} symmetry point groups. The orbitals are calculated at the QCISD and MP4SDQ levels of theory with the aug-cc-pVTZ basis set, and the geometries were reported by Bell and Wright.[35]

in the 390 nm O_2^-·H_2O image [Figure 1d]. However, this image has a more anisotropic angular distribution as compared to 780 nm, reflecting a qualitative trend similar to that in O_2^-.

The photoelectron spectra extracted from the O_2^-·H_2O photoelectron images are shown in Figure 2c and d for 780 and 390 nm, respectively. At 780 nm, the signal peaks at eBE $\approx$ 1.5 eV, close to the photon energy. At 390 nm, the spectrum consists of two overlapping congested bands peaking in the vicinity of 1.9 and 2.8 eV, consistent with the measurements by the groups of Johnson[16] and Continetti.[19] These bands are attributed to the following dissociative detachment processes:

$$O_2^-\cdot H_2O + h\nu \rightarrow O_2(X\,^3\Sigma_g^-) + H_2O + \bar{e}\,(\text{eKE}) \quad (2a)$$

$$O_2(a\,^1\Delta_g) + H_2O + \bar{e}\,(\text{eKE}) \quad (2b)$$

Unlike O_2^-, the intensity of the O_2^-·H_2O photoelectron images peaks near the image centers and the corresponding spectra at both wavelengths studied show fast-rising signals near zero eKE.

Figure 3a and b compares the anisotropy parameters obtained for superoxide with those for O_2^-·H_2O at 780 nm and in the vicinity of 390 nm, respectively. Because the adiabatic detachment energy of O_2^-·H_2O (1.42 ± 0.05 eV)[19] exceeds the corresponding value for O_2^- (0.448 ± 0.006 eV),[21] photodetachment of the hydrated anion spans a narrower eKE range. Nonetheless, at both 780 and 390 nm, the eKE-dependent β values for O_2^-·H_2O fall close to the corresponding O_2^- results within the experimental uncertainty. As in the O_2^- case, the 780 and 390 nm data for O_2^-·H_2O follow diverging β(eKE) trends.

4. Discussion

Theoretical studies indicate that the O_2^-·H_2O cluster anion has two low-energy isomers, both of which have planar equilibrium geometries corresponding to the C_s and C_{2v} symmetry point groups, respectively.[30−35,37,39−43] Depending on the orientation of the $2p\pi_g^*$ HOMO of O_2^- with respect to the water molecule, the electronic symmetries of the cluster anion correspond to the $^2A''$ and $^2A'$ states for the C_s isomer and $^2A_2$ and $^2B_2$ for the C_{2v} isomer. Calculations predict the $^2A''$ and $^2A_2$ states to have lowest energies for the corresponding geometric forms of the cluster anion.[30,35]

Because of the similar equilibrium energies and low potential barrier between the C_s and C_{2v} forms of O_2^-·H_2O, both isomers are expected to coexist in the ion beam and contribute to the photoelectron images. The HOMOs of O_2^- and the C_s ($^2A''$) and C_{2v} ($^2A_2$) structures of O_2^-·H_2O are represented in Figure 4a−c. The orbitals were calculated for the geometries reported by Bell and Wright[35] at the QCISD and MP4SDQ levels of

theory with the aug-cc-pVTZ basis set, using the Gaussian 03 program suite.[62]

The calculations indicate that the HOMOs of both $O_2^-\cdot H_2O$ structures retain the main features of the O_2^- HOMO. Therefore, the photodetachment from $O_2^-\cdot H_2O$ can be considered by approximating the parent cluster orbital as the core O_2^- HOMO. Indeed, in Figure 3 there is a good agreement between the β(eKE) trends for $O_2^-\cdot H_2O$ and O_2^-. The observed anisotropy values are also consistent with the past experimental studies of O_2^- photodetachment,[63,64] as well as theoretical expectations.[22,65,66] The photodetachment from a π_g* molecular orbital has been studied extensively in the past, adopting different theoretical frameworks.[22,45] Although the variation of the anisotropy parameter β with eKE within the Cooper−Zare central-potential model is not intuitive, qualitative symmetry-related aspects of π_g^{-1} photodetachment were discussed by our group on the example of S_2^-.[45] The same symmetry considerations, generally predicting negative values of β in a moderate eKE range, also apply in the case of O_2^-.

Upon photodetachment, $O_2^-\cdot H_2O$ dissociates according to eqs 2a and 2b. The photodetachment occurs at the O_2^- moiety via a Franck−Condon excitation to an $O_2\cdot H_2O$ neutral potential energy surface, which is weakly repulsive along the intermolecular coordinate.[19] The dissociation process is expected to have no effect on the photodetachment dynamics,[19] and the photoelectron angular distributions should therefore reflect the $O_2^- \rightarrow O_2 + \bar{e}$ process. The agreement between the experimental O_2^- and $O_2^-\cdot H_2O$ β(eKE) curves is therefore expected in each of the wavelength regions studied.

Finally, we note that the photoelectron spectra of $O_2^-\cdot H_2O$ shown in Figure 2c and d are characterized by a rapid, steplike signal rise in the near-zero-eKE region. This observation contrasts the gradual signal onset with increasing eKE observed at both wavelengths studied in the O_2^- case [Figure 2a and b]. To shed light on this difference, we note that in O_2^- slow-electron detachment is dominated by p waves,[20,22] because no s partial waves are allowed within the electric-dipole approximation for electrons originating from the d-like π_g* parent orbital. The p waves are susceptible to the centrifugal effects dictated by the Wigner law,[54,55] as discussed in section 3. In the $O_2^-\cdot H_2O$ cluster, the addition of H_2O lowers the HOMO symmetry, formally allowing s waves, which do not experience a centrifugal barrier. Hence, even small-amplitude s waves may contribute significantly to the yield of slow photoelectrons. The angular distributions, on the other hand, will be less affected by minor s wave contributions, as they are most important at low eKEs, where the anisotropy parameter β is already close to zero.

We also cannot rule out possible non-Wigner behavior in the $O_2^-\cdot H_2O$ case, due to the long-range charge−dipole interaction between the departing electron and the neutral core of the cluster.[54,55,57,67,68] To test this hypothesis, we calculated the dipole moment of neutral cluster in the ground electronic state at the anion geometry. The anion geometries reported by Wright and Bell,[35] corresponding to minimum energy for a given level of theory, were used to determine the neutral dipole moments summarized in Table 2. For both $O_2^-\cdot H_2O$ isomers, at all levels of theory, the neutral dipole moment is predicted to exceed 2.3 D, giving weight to the possibility that the long-range electron−dipole interaction may indeed be responsible for the lowering of the centrifugal barrier in the photodetachment of hydrated superoxide, increasing the relative yield of slow photoelectrons. The implications of the availability of slow electrons for gas-phase, condensed-phase, and biological systems are well documented.[69−76] For example, the high capture cross-section for low kinetic energy electrons increases the possibility of backbone fragmentation in biological molecules[77,78] and adsorbed film damage in the condensed phase.[79]

TABLE 2: Calculated Dipole Moments of the $O_2\cdot H_2O$ Neutral at the C_s and C_{2v} Equilibrium Geometries of the Anion

	dipole moment (debye)	
method[a]	C_s	C_{2v}
B3LYP	2.31	2.62
MP4SDQ	2.58	2.66
QCISD	2.69	2.65
MP2		2.73

[a] Dunning's aug-cc-pVTZ basis set was used at all levels of theory.

5. Conclusions

The effect of monohydration on the electronic structure and photodetachment dynamics of the superoxide radical anion was studied by photoelectron imaging spectroscopy at 1.59 and 3.18 eV photon energies. Overall, the hydration is found to have a pronounced effect on the photoelectron energy spectra, but not on the angular distributions.

First, the broad and congested transitions in the $O_2^-\cdot H_2O$ photoelectron spectra are shifted toward larger eBEs with respect to the vibrationally resolved transitions in O_2^-, in agreement with previous work.[15] The spectral congestion is attributed to the additional degrees of freedom present in the hydrated cluster anion and the dissociative nature of the detachment process, while the spectral shift is due to the solvation stabilization of the core negative ion within the cluster.

Second, at both 1.59 and 3.18 eV photon energies the photoelectrons emitted from $O_2^-\cdot H_2O$ exhibit angular distributions that are quantitatively similar to those obtained for bare O_2^- at the same detachment wavelength and in the same electron kinetic energy range. This observation confirms that the excess electron in $O_2^-\cdot H_2O$ resides in an orbital that is similar in structure to the $2p\pi_g$* HOMO of O_2^-.

Third, as compared to the O_2^- case, the photodetachment of $O_2^-\cdot H_2O$ exhibits a faster signal rise from the zero-eKE limit. This behavior is attributed to the long-range charge−dipole attraction between the departing electron and $O_2\cdot H_2O$, counteracting the centrifugal barrier to p wave photodetachment, and contributions from s wave photodetachment, which are forbidden in O_2^- but cannot be ruled out for $O_2^-\cdot H_2O$.

Acknowledgment. We would like to thank Richard Mabbs, Kent M. Ervin, Daniel M. Neumark, and W. Carl Lineberger for extensive discussions and Robert E. Continetti for sending us a copy of the manuscript in ref 26 prior to publication. This work is supported by the National Science Foundation (NSF grant no. CHE-0134631) and the David and Lucile Packard Foundation (Packard Fellowship for Science and Engineering). In addition, L.K.S. thanks the Department of Chemistry, University of Arizona, for support under the NSF Research Experience for Undergraduates (REU) program in the summer of 2005.

References and Notes

(1) Lovell, M. A.; Xie, C. S.; Markesbery, W. R. *Brain Res.* **2000**, *855*, 116.

(2) Beckman, K. B.; Ames, B. N. *Physiol. Rev.* **1998**, *78*, 547.

(3) Ferguson, E. E.; Fehsenfeld, F. C.; Albritton, D. L. Ion Chemistry of the Earth's Atmosphere. In *Gas-Phase Ion Chemistry*; Bowers, M. T., Ed.; Academic Press: New York, 1979; Vol. 1, p 45.

(4) Ferguson, E. E.; Arnold, F. *Acc. Chem. Res.* **1981**, *14*, 327.
(5) Schneider, H.; Boese, A. D.; Weber, J. M. *J. Chem. Phys.* **2005**, *123*.
(6) Cabane, M.; Playe, P. *J. Aerosol Sci.* **1980**, *11*, 475.
(7) Ferguson, E. E. *Can. J. Chem.* **1969**, *47*, 1815.
(8) Adams, N. G.; Bohme, D. K.; Dunkin, D. B.; Fehsenfeld, F. C.; Ferguson, E. E. *J. Chem. Phys.* **1970**, *52*, 3133.
(9) Arshadi, M.; Kebarle, P. *J. Phys. Chem.* **1970**, *74*, 1483.
(10) Wincel, H.; Mereand, E.; Castleman, A. W. *J. Phys. Chem.* **1995**, *99*, 1792.
(11) Fahey, D. W.; Bohringer, H.; Fehsenfeld, F. C.; Ferguson, E. E. *J. Chem. Phys.* **1982**, *76*, 1799.
(12) Fehsenfeld, F. C.; Ferguson, E. E. *J. Chem. Phys.* **1974**, *61*, 3181.
(13) Weber, J. M.; Kelley, J. A.; Nielsen, S. B.; Ayotte, P.; Johnson, M. A. *Science* **2000**, *287*, 2461.
(14) Weber, J. M.; Kelley, J. A.; Robertson, W. H.; Johnson, M. A. *J. Chem. Phys.* **2001**, *114*, 2698.
(15) Lavrich, D. J.; Buntine, M. A.; Serxner, D.; Johnson, M. A. *J. Chem. Phys.* **1993**, *99*, 5910.
(16) Buntine, M. A.; Lavrich, D. J.; Dessent, C. E.; Scarton, M. G.; Johnson, M. A. *Chem. Phys. Lett.* **1993**, *216*, 471.
(17) Lavrich, D. J.; Buntine, M. A.; Serxner, D.; Johnson, M. A. *J. Phys. Chem.* **1995**, *99*, 8453.
(18) Sherwood, C. R.; Continetti, R. E. *Chem. Phys. Lett.* **1996**, *258*, 171.
(19) Luong, A. K.; Clements, T. G.; Resat, M. S.; Continetti, R. E. *J. Chem. Phys.* **2001**, *114*, 3449.
(20) Burch, D. S.; Smith, S. J.; Branscomb, L. M. *Phys. Rev.* **1958**, *112*, 171.
(21) Ervin, K. M.; Anusiewicz, W.; Skurski, P.; Simons, J.; Lineberger, W. C. *J. Phys. Chem. A* **2003**, *107*, 8521.
(22) Reed, K. J.; Zimmerman, A. H.; Andersen, H. C.; Brauman, J. I. *J. Chem. Phys.* **1976**, *64*, 1368.
(23) Dinu, L.; Groenenboom, G. C.; van der Zande, W. J. *J. Chem. Phys.* **2003**, *119*, 8864.
(24) Clements, T. G.; Luong, A. K.; Deyerl, H. J.; Continetti, R. E. *J. Chem. Phys.* **2001**, *114*, 8436.
(25) Bowen, M. S.; Becucci, M.; Continetti, R. E. *J. Phys. Chem. A* **2005**, *109*, 11781.
(26) Bowen, M. S.; Becucci, M.; Continetti, R. E. *J. Chem. Phys.*, submitted.
(27) Surber, E.; Sanov, A. *J. Chem. Phys.* **2002**, *116*, 5921.
(28) Mabbs, R.; Surber, E.; Sanov, A. *J. Chem. Phys.* **2005**, *122*, 054308.
(29) Surber, E.; Mabbs, R.; Habteyes, T.; Sanov, A. *J. Phys. Chem. A* **2005**, *109*, 4452.
(30) Curtiss, L. A.; Melendres, C. A.; Reed, A. E.; Weinhold, F. *J. Comput. Chem.* **1986**, *7*, 294.
(31) Ohta, K.; Morokuma, K. *J. Phys. Chem.* **1987**, *91*, 401.
(32) Lee, E. P. F.; Dyke, J. M. *Mol. Phys.* **1991**, *74*, 333.
(33) Robinson, E. M. C.; Holstein, W. L.; Stewart, G. M.; Buntine, M. A. *Phys. Chem. Chem. Phys.* **1999**, *1*, 3961.
(34) Lee, H. M.; Kim, K. S. *Mol. Phys.* **2002**, *100*, 875.
(35) Bell, A. J.; Wright, T. G. *Phys. Chem. Chem. Phys.* **2004**, *6*, 4385.
(36) Seta, T.; Yamamoto, M.; Nishioka, M.; Sadakata, M. *J. Phys. Chem. A* **2003**, *107*, 962.
(37) Kuo, I. F. W.; Tobias, D. J. *J. Phys. Chem. A* **2002**, *106*, 10969.
(38) Antonchenko, V. Y.; Kryachko, E. S. *J. Phys. Chem. A* **2005**, *109*, 3052.
(39) Pilipchuk, V. G.; Smolinskii, V. V.; Shchekatolina, S. A. *J. Struct. Chem.* **1988**, *29*, 787.
(40) Pilipchuk, V. G.; Smolinskii, V. V.; Shchekatolina, S. A. *J. Struct. Chem.* **1990**, *31*, 649.
(41) Pilipchuk, V. G.; Smolinskii, V. V.; Shchekatolina, S. A. *Zh. Fiz. Khim.* **1990**, *64*, 1391.
(42) Lopez, J. P.; Albright, T. A.; McCammon, J. A. *Chem. Phys. Lett.* **1986**, *125*, 454.
(43) Lopez, J. P. *J. Comput. Chem.* **1989**, *10*, 55.
(44) Eppink, A. T. J. B.; Parker, D. H. *Rev. Sci. Instrum.* **1997**, *68*, 3477.
(45) Surber, E.; Mabbs, R.; Sanov, A. *J. Phys. Chem. A* **2003**, *107*, 8215.
(46) Wiley, W. C.; McLaren, I. H. *Rev. Sci. Instrum.* **1955**, *26*, 1150.
(47) Heck, A. J. R.; Chandler, D. W. *Annu. Rev. Phys. Chem.* **1995**, *46*, 335.
(48) Dribinski, V.; Ossadtchi, A.; Mandelshtam, V. A.; Reisler, H. *Rev. Sci. Instrum.* **2002**, *73*, 2634.
(49) Krupenie, P. H. *J. Phys. Chem. Ref. Data* **1972**, *1*, 423.
(50) Herzberg, L.; Herzberg, G. *Astrophys. J.* **1947**, *105*, 353.
(51) Nieh, J. C.; Valentini, J. J. *J. Phys. Chem.* **1987**, *91*, 1370.
(52) Babcock, H. D.; Herzberg, L. *Astrophys. J.* **1948**, *108*, 167.
(53) O'Brien, L. C.; Cao, H.; O'Brien, J. J. *J. Mol. Spectrosc.* **2001**, *207*, 99.
(54) Wigner, E. P. *Phys. Rev.* **1948**, *73*, 1002.
(55) Lineberger, W. C.; Hotop, H.; Patterson, T. A. Photodetachment Threshold Processes. In *Electron and Photon Interactions with Atoms*; Kleinpoppen, H., McDowell, M. R. C., Eds.; Plenum Publishing Corporation: New York, 1976; p 125.
(56) Mead, R. D.; Lykke, K. R.; Lineberger, W. C. Photodetachment Threshold Laws. In *Electronic and Atomic Collisions*; Eichler, J., Hertel, I. V., Stolterfoht, N., Eds.; Elsevier: New York, 1984; p 721.
(57) Farley, J. W. *Phys. Rev. A* **1989**, *40*, 6286.
(58) Cooper, J.; Zare, R. N. *J. Chem. Phys.* **1968**, *48*, 942.
(59) Cooper, J.; Zare, R. N. *J. Chem. Phys.* **1968**, *49*, 4252.
(60) Hanstorp, D.; Bengtsson, C.; Larson, D. J. *Phys. Rev. A* **1989**, *40*, 670.
(61) Gilles, M. K.; Ervin, K. M.; Ho, J.; Lineberger, W. C. *J. Phys. Chem.* **1992**, *96*, 1130.
(62) Frisch, M. J.; et al. *Gaussian 03*, revision B.01; Gaussian, Inc.: Wallingford, CT, 2004.
(63) Burch, D. S.; Smith, S. J.; Branscomb, L. M. *Phys. Rev.* **1958**, *112*, 171.
(64) Celotta, R. J.; Bennett, R. A.; Levine, J.; Hall, J. L.; Siegel, M. W. *Phys. Rev. A* **1972**, *6*, 631.
(65) Stehman, R. M.; Woo, S. B. *Bull. Am. Phys. Soc.* **1978**, *23*, 155.
(66) Stehman, R. M.; Woo, S. B. *Phys. Rev. A* **1981**, *23*, 2866.
(67) O'Malley, T. F. *Phys. Rev.* **1965**, *137*, A1668.
(68) Smith, J. R.; Kim, J. B.; Lineberger, W. C. *Phys. Rev. A* **1997**, *55*, 2036.
(69) Balog, R.; Langer, J.; Gohlke, S.; Stano, M.; Abdoul-Carime, H.; Illenberger, E. *Int. J. Mass Spectrom.* **2004**, *233*, 267.
(70) Sanche, L. *Eur. Phys. J. D* **2005**, *35*, 367.
(71) Duwez, A. S. *J. Electron Spectrosc. Relat. Phenom.* **2004**, *134*, 97.
(72) Zharnikov, M.; Frey, S.; Heister, K.; Grunze, M. *Langmuir* **2000**, *16*, 2697.
(73) Laiho, T.; Leiro, J. A.; Heinonen, M. H.; Mattila, S. S.; Lukkari, J. *J. Electron Spectrosc. Relat. Phenom.* **2005**, *142*, 105.
(74) Anusiewicz, I.; Berdys-Kochanska, J.; Skurski, P.; Simons, J. *J. Phys. Chem. A* **2006**, *110*, 1261.
(75) Anusiewicz, I.; Jasionowski, M.; Skurski, P.; Simons, J. *J. Phys. Chem. A* **2005**, *109*, 11332.
(76) Anusiewicz, W.; Berdys-Kochanska, J.; Simons, J. *J. Phys. Chem. A* **2005**, *109*, 5801.
(77) Boudaiffa, B.; Cloutier, P.; Hunting, D.; Huels, M. A.; Sanche, L. *Med. Sci.* **2000**, *16*, 1281.
(78) Boudaiffa, B.; Cloutier, P.; Hunting, D.; Huels, M. A.; Sanche, L. *Science* **2000**, *287*, 1658.
(79) Pascual, J. I.; Lorente, N.; Song, Z.; Conrad, H.; Rust, H. P. *Nature* **2003**, *423*, 525.
(80) Cheung, A. S. C.; Yoshino, K.; Esmond, J. R.; Parkinson, W. H. *J. Mol. Spectrosc.* **1996**, *178*, 66.